Quantum Ratcheted Photophysics in Energy Transport

Pallavi Bhattacharyya^{†,‡,¶} and Graham R. Fleming^{*,†,‡,¶}

†Department of Chemistry, University of California, Berkeley 94720, USA

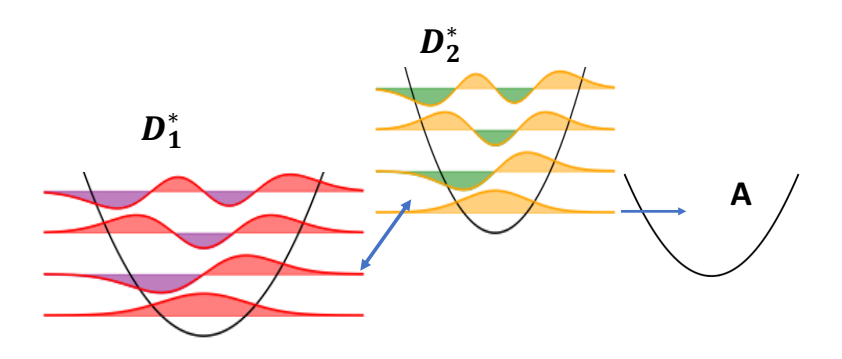
‡Molecular Biophysics and Integrated Bioimaging Division, Lawrence Berkeley National

Lab, Berkeley, California 94720, USA

¶Kavli Energy Nanosciences Institute at Berkeley, Berkeley, California 94720, USA

E-mail: grfleming@lbl.gov

Abstract



In this paper, we explore the scope of vibrations as quantum ratchets that serve as non-thermal routes to achieving population transport in systems where excitation transport between molecules is otherwise energetically unfavorable. In addition to their role as channels of transport, we investigate the effect of resonance of the vibrations, that are described by Huang Rhys mixing, with excitonic energy gaps, that leads to strongly mixed vibronic excitons. Finally, we explore the interplay of resonance and Huang Rhys mixing with electronic coupling between the molecules, in the presence of a dissipative bath, in optimizing transport in such systems. We find that while resonance is desirable, a moderate electronic coupling has a stronger positive effect in contrast to a large electronic coupling which results in delocalised excitations across molecules and hampers unidirectional transport. We also report a special resonance regime that is able to circumvent the transport problems arising from large electronic couplings.

To exploit coherences to aid the architecture of synthetic light-harvesting machinery is an area of rapidly proliferating interest. Coherences in molecular systems occur due to large electronic couplings between molecules, resulting in delocalised excitations/excitons, that offer a route to manipulating molecular systems away from bath-induced dissipation and Boltzmann statistics. Theoretical calculations by Ishizaki and Fleming suggest that quantum coherence could be beneficial in overcoming local energy traps, thus mediating efficient EET (electronic energy transport) in the Fenna-Matthews-Olson photosynthetic complex. ¹ A key benefit, thus, can be realized in the potential to control molecular dynamics and direct energy/charge transport by harvesting coherences. Conjugated molecular aggregates, for instance, are promising candidates for such control, due to the extended π -stacking prevalent in such systems due to the highly ordered microscopic assemblies. A major disadvantage, however, is posed by the fragility of molecular coherences, since they are extremely susceptible to destruction by their surroundings/bath. As a consequence, disorder and imperfections in the molecular assemblies will diminish the exciton length and limit coherence. A plethora of theoretical studies report that vibrationally enhanced transfer achieves an optimal transfer efficiency in such scenarios. ^{2,3} Also, vibrations, if they are resonant with an excitonic energy gap and are strongly coupled to the electronic transition, have the capacity to provide a means to circumvent this difficulty. This is because the excitation can switch back and forth between the exciton and the vibration that is less susceptible to decoherence, resulting in longer-lived coherences. 4-7 For instance, calculations by Plenio and coworkers suggest that

non-equilibrium processes due to spectrally sharp vibrational modes can effectively compete with dissipative pathways induced by the thermal bath. 8 In another work reported by Cao and coworkers, it is proposed that underdamped vibrations resonant with energy gaps in the system can drive excitation transport, in addition to retention of coherences for longer timescales. The work by Bennett et al. suggests that incoherent vibronic transport results in more efficient excitation transfer, compared to coherent transport, if the energetic disorder is greater then the coupling between the donor and the vibrationally excited states on the acceptor. ¹⁰ A recent work from our group suggests that underdamped vibrations, resonant with excitonic energy gaps in the LHCII complex, can drive population transport across large energy gaps that are thermally inaccessible. 11 Therefore, vibrations and coherences are important tools that can be exploited for the design of efficient energy-harvesting and charge transport devices. Key advances that utilize such design principles are actively studied by Therien and coworkers, where they report the synthesis of "supermolecules", that are composed of highly conjugated and strongly coupled PZn_n porphyrin arrays. 12-21 The studies suggest that these molecules enjoy resonances between vibrations and excitons, as well as strong vibronic coupling between vibrations and excitonic transitions. This is expected to lead to vibronic mixing, that could pave the way to robust coherences. The studies also report transition dipole moments for the $S_0 \to S_1$ transition that increase progressively as the number of PZn_n units increase. A key manifestation of this is large electronic couplings across the porphyrin assemblies, that again ensures large exciton coherence lengths. In this work, we explore the interplay between resonance and electronic coupling and Huang Rhys mixing, in an effort to formulate design principles that would ensure efficient energy-harvesting in synthetic devices. We specifically investigate the role of vibrations as non-thermal routes to ratcheting populations between molecules.

In this work, our focus is on the scope of quantum ratcheted photophysics in model systems where energy transport is otherwise energetically unfavorable. This is demonstrated in figure 1(a), where the objective is to achieve a fast and efficient transport of excitation

from the electronically excited donor molecule D_1^* to an acceptor molecule A. A favorable electronic coupling between D_1^* and A would potentially lead to coherent transport, but the spatial separation between them is large, resulting in small electrostatic couplings. The other possibility is incoherent Forster transport, that again is unfavorable due a large spatial separation. Also, the energetic constraint $E_{D_1} < E_A$ necessitates an uphill transport from D_1^* to A. This pathway is thermally inaccessible if the energy gap $\Delta E_{A,D_1} > k_B T$, where T is the temperature of the thermal bath. To circumvent the transport problems, we use a second intermediate donor molecule D_2 , that acts as a bridge between D_1 and A, given that we have an efficient, non-thermal route to transporting excitation from D_1^* to D_2^* . Here, D_2^* is the electronically excited S_1 state on D_2 . The excitation, then, undergoes a downhill transport from D_2^* to A. We propose to accomplish this by exploiting a vibrational mode that ratchets population from D_1^* to D_2^* through the mechanism discussed below. Denoting the electronic excitons formed from a two-level electronic Hamiltonian defined by the S_1 states of D_1^* and D_2^* as m and n, the transport between m and n can be effectively mediated by a vibrational mode that is resonant/quasi-resonant with the excitonic energy gap $\Delta \epsilon_{mn}$. In the simplest model, the presence of the vibrational mode is incorporated through its Huang-Rhys mixing. We consider A to be an energy sink, thus the energy transport from D_2^* to A is unidirectional and irreversible. Therefore, for a minimal description of the system Hamiltonian that adequately describes quantum ratcheting, we will consider only the electronic/vibronic states of D_1^* and D_2^* , while the excitation transfer from D_2^* to Ais easily evaluated by a simple kinetic equation. We investigate the interplay between the Huang-Rhys mixing, the resonance/quasi-resonance of the vibrational mode with the excitonic energy gap and coherence, arising from the electronic coupling between D_1^* and D_2^* , in dictating the transport between these molecules, in the presence of a dissipative bath. It is important to note here that the relaxation of the vibrationally excited state on D_1^* , due to its interaction with the bath, serves as a competing pathway to transport from D_1^* to D_2^* . In our calculations, we incorporate the effects of such relaxation.

To model the ratcheting dynamics, we define a system Hamiltonian that explicitly includes the vibrational mode, along with the electronically excited states of D_1 and D_2 . For efficient yet adequate calculations, we define our local basis as follows: $\{|D_1v_{D_1,0}^e, v_{D_2,0}^g\rangle, |D_1v_{D_1,0}^e, v_{D_2,0}^e\rangle, |D_2v_{D_1,0}^g, v_{D_2,0}^e\rangle, |D_2v_{D_1,0}^g, v_{D_2,0}^e\rangle, |$ where the first term in the ket indicates the species that is electronically excited. $v_{D,l}^k$ contains the vibrational information on the donor species $D(D \in \{D_1, D_2\})$, given by the vibrational quantum number l in the k electronic state, where $k \in \{g, e\}$, implying the ground and excited electronic states, respectively. The prime symbol "'" on the vibrational state l on e indicates that this vibrational wavefunction is structurally different from its counterpart on g due to a different charge distribution on e. It is worth emphasizing that it is always possible to add more vibrational information to the Hamiltonian, by incorporating a larger vibrational basis. In our studies, however, the focus is the ratcheting dynamics stemming from the excitation of the vibrational mode on D_1^* that places D_1 at a higher energy compared to D_2^* and the subsequent excitation transfer due to resonance. Therefore, including up to the first vibrationally excited state on D_1^* , while considering the vibrational ground state on D_2^* , is adequate to infer more about the ratcheting photophysics.

The vibronic Hamiltonian of the system, with respect to the local basis described above, can be written as follows:

$$H_{sys} = \begin{pmatrix} E_{D_1} & 0 & JS_{00'}^{D_1}S_{00'}^{D_2} \\ 0 & E_{D_1} + \Omega & JS_{01'}^{D_1}S_{00'}^{D_2} \\ JS_{00'}^{D_1}S_{00'}^{D_2} & JS_{01'}^{D_1}S_{00'}^{D_2} & E_{D_2} \end{pmatrix}.$$
 (1)

Here, E_{D_1} and E_{D_2} are the energies of the ground vibrational states in the electronically excited e states for D_1 and D_2 , respectively. The vibrational mode has a frequency Ω , J is the electronic coupling between D_1 and D_2 , and $S_{vv'}^D$ measures the overlap between the nuclear wavefunctions describing the vibrational states v (residing on the ground electronic state) and v' (residing on the electronically excited state) respectively, on D ($D \in \{D_1, D_2\}$) and is expressed in terms of the Huang-Rhys factors. While H_{sys} describes the electronic

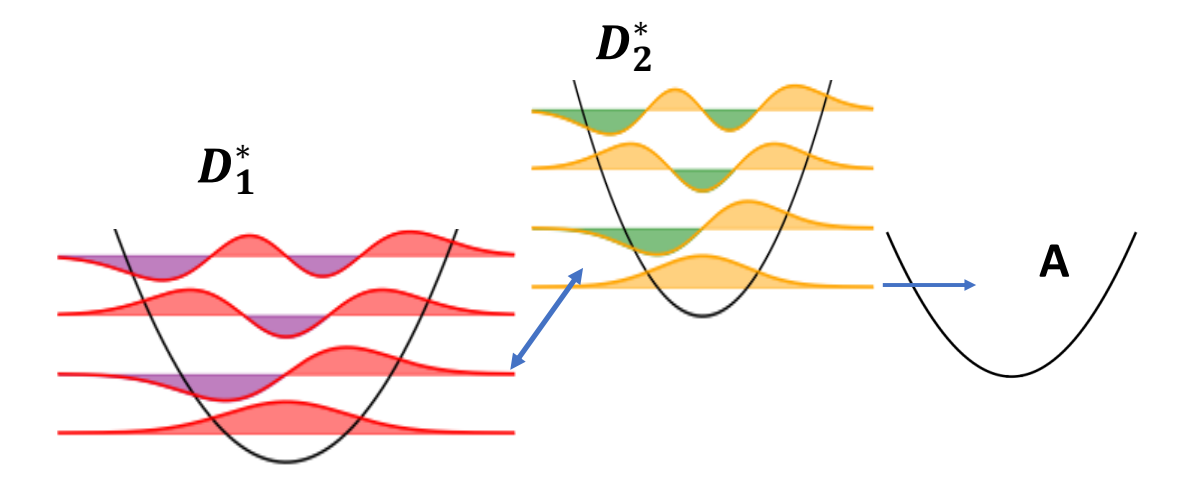


Figure 1: A schematic depicting ratcheted energy transport. Direct transfer of excitation from D_1^* to A is unfavorable, both energetically and owing to a large spatial separation between them. To address this, we use an intermediate molecule D_2 , that is placed between D_1 and A. A vibration is used as a quantum ratchet to achieve non-thermal transport of population from D_1^* to D_2^* , followed by a unidirectional decay to A, that acts as an energy sink. The relaxation of the vibrational mode on D_1^* , due to its interaction with the bath, serves as a competing pathway.

and vibrational excitations, we use the following total Hamiltonian H that incorporates the phonons, also referred to as the bath/environment, that are modeled as harmonic oscillators in H_{ph} , and the system-bath interaction described by H_{sys-ph} .

$$H = H_{sus} + H_{sus-ph} + H_{ph}, \tag{2}$$

where

$$H_{ph} = \sum_{j,k} \left(\frac{p_{jk}^2}{2m_{jk}} + \frac{1}{2} m_{jk} q_{jk}^2 \omega_{jk}^2 \right), \tag{3}$$

and $H_{sys-ph} = \sum_{j} Q_j \mid j \rangle \langle j \mid$, where

$$Q_j = \sum_k m_{jk} \nu_{jk} q_{jk}. \tag{4}$$

Here, m_{jk} , q_{jk} , p_{jk} and ω_{jk} describe the mass, position, momentum and angular frequency, respectively, of the k^{th} bath oscillator pertaining to the j^{th} system state. The system-bath interaction, in Eq. 4, is diagonal with respect to the local basis and is considered to be adequately described by a linear dependence of the position coordinate q_{jk} . ν_{jk} describes the coupling strength of the k^{th} oscillator with the j^{th} site.

For simulating dynamics, we will employ a reduced density matrix description of the system and use a near-analytic approximate approach. $^{22-24}$ This approach uses a unitary mapping that transforms to a stationary adiabatic basis, formed by diagonalizing $H_{sys} + H_{sys-ph}$, and frozen at the equilibrium geometry. The technical definition for stationary adiabatic states, therefore, differs from that of excitons, that are eigenstates formed by diagonalizing only the system Hamiltonian and do not reflect any contribution from the bath. It is important to note here that though they differ in their definitions, the energies of the excitons formed by diagonalizing the system Hamiltonian are the same as those of the stationary adiabatic states. 11

The chief benefit of the unitary mapping arises from a decoupling between decoherence,

described by fluctuations in the energies of the dynamically evolving adiabatic states due to shifting of the bath position coordinates, and phonon-mediated population relaxation, described by a derivative operator that drives a change in electronic state, in conjunction with bath momenta. This is followed by a nonperturbative treatment of decoherence, that captures the effects of the dynamically fluctuating energies of the stationary adiabatic states (see eqns. 6 and 7), while the population relaxation is described perturbatively. The method has been described in rigorous detail in previous work, therefore we will only discuss the final expression for the reduced density operator we use to describe the system.

While $|\alpha\rangle\langle\alpha|$ describes the initial density operator at t=0, where α denotes a local state, we intend to determine the extent of overlap of the excitation at time t with the local basis coherence $|\gamma\rangle\langle\beta|$. In the expression below, m, n, m' and n' denote the stationary adiabatic states, ϵ_n denoting the energy of the stationary adiabatic state n. The bath is described by the spectral density function $S(\omega)$, defined below, at temperature T.

$$\rho_{\beta\gamma}(t) \approx \sum_{m,n,m'} \langle \beta \mid m \rangle \langle n \mid \alpha \rangle \langle \alpha \mid n \rangle \langle m' \mid \gamma \rangle p_{mm',nn}(t) +$$

$$\sum_{m,n,n',m'} \langle \beta \mid m \rangle \langle n \mid \alpha \rangle \langle \alpha \mid n' \rangle \langle m' \mid \gamma \rangle p_{mm',nn'}(t)$$

$$\times e^{-i\epsilon_{nn'}t} e^{-\phi_{n,n'}(t)}.$$
(5)

Here, $\epsilon_{nn'} = \epsilon_n^0 - \epsilon_{n'}^0$, $\phi_{n,n'}(t) = Re[\phi_{n,n'}(t)] + i \ Im[\phi_{n,n'}(t)]$, where $\phi_{n,n'}(t)$ describes the effects of decoherence, with the real and imaginary components given as:

$$Re[\phi_{n,n'}(t)] = \int_0^\infty d\omega S(\omega) \frac{1 - \cos(\omega t)}{\omega^2} \coth\left(\frac{\omega}{2k_B T}\right) \times \sum_j \left(\frac{\partial \epsilon_n}{\partial Q_j} - \frac{\partial \epsilon_{n'}}{\partial Q_j}\right)_{Q_j = 0}^2, \tag{6}$$

and

$$Im[\phi_{n,n'}(t)] = \int_0^\infty d\omega S(\omega) \frac{\sin(\omega t) - \omega t}{\omega^2} \times \sum_j \left[\left(\frac{\partial \epsilon_n}{\partial Q_j} \right)_{Q_j = 0}^2 - \left(\frac{\partial \epsilon_{n'}}{\partial Q_j} \right)_{Q_j = 0}^2 \right].$$
(7)

Here, $S(\omega)$ is the spectral density of the environment, defined as:

$$S(\omega) = \sum_{k} \frac{m_{jk} \nu_{jk}^2}{2\omega_{jk}} \delta(\omega - \omega_{jk}). \tag{8}$$

While $e^{-\phi_{n,n'}(t)}$ is evaluated nonperturbatively and describes the effects of decoherence, the term $p_{mm',nn'}(t)$ addresses the effects of relaxation arising from a perturbative treatment of the nonadiabatic derivative operator, in conjunction with bath momenta and is evaluated using a Markovian master equation, that is solved using matrix algebra. The relaxation rates, arising from the perturbative treatment of relaxation, for a pair of stationary adiabatic states m and m' are given as:

$$\Gamma_{mm'} = 2\pi \frac{S(\omega_{mm'})}{e^{\omega_{mm'}/k_BT} - 1} \sum_{j} (\langle m' \mid j \rangle \langle j \mid m \rangle)^2, \tag{9}$$

and

$$\Gamma_{m'm} = e^{\omega_{mm'}/k_B T} \Gamma_{mm'}. \tag{10}$$

In the above expression, $\omega_{mm'} > 0$, where $\omega_{mm'} = \epsilon_m^0 - \epsilon_{m'}^0$.

We will now apply the above formalism to investigate quantum ratcheted energy transport in various model systems. In our discussion forward, we will loosely refer to stationary adiabatic states as adiabatic states, for convenience. However, it is important to keep in mind the subtle distinction between excitons and adiabatic states.

Table 1 enumerates the system parameters for the various models we consider. In figures 2 and 4, we demonstrate the energy level diagrams for each of these models, where l_1 , l_2 and l_3

label the local states. l_1 and l_2 are localized on D_1 and label the states $|D_1 v_{D_1,0}^e, v_{D_2,0}^e\rangle$ and $|D_1 v_{D_1,1}^e, v_{D_2,0}^e\rangle$, respectively. l_3 is localized on D_2 and labels the state $|D_2 v_{D_1,0}^e, v_{D_2,0}^e\rangle$. a_1 , a_2 and a_3 label the stationary adiabatic states. We list the eigenvector contributions for the adiabatic states with respect to the local states, for all the six models, in the supplementary information. The quantity we wish to investigate here is the population transport to l_3 , while l_2 is considered the initial seat of excitation. This is achieved by directly exciting l_2 from the ground electronic state, by using a UV-vis radiation field of suitable frequency. A second way of placing the initial population at l_2 is by first exciting l_1 using a UV-vis pulse, followed by an IR pulse that creates the vibrational excitation, leading to the population being transported from l_1 to l_2 . Therefore, for ratcheted photophysics, we consider the temporal evolution of population, considering l_2 to be the initial state.

For model 1, the vibronic system Hamiltonian and the energy level diagram are depicted in Table 1: System parameters for the various models we consider. $\Delta E_{D_2,D_1}$ denotes the difference between the bare electronic excitation energies on D_2 and D_1 , respectively. J denotes the electronic coupling between D_1 and D_2 , and Ω is the excitation frequency of the vibrational mode.

	Model 1	Model 2	Model 3	Model 4	Model 5	Model 6
$\Delta E_{D_2,D_1} \ (cm^{-1})$	800	800	400	800	400	400
$J(cm^{-1})$	200	200	400	200	400	400
$\Omega (cm^{-1})$	895	800	895	700	646	646
σ	0.01	0.01	0.01	0.01	0.01	0.1

Figure 2(a). If we consider the electronic-only Hamiltonian formed by the basis states $|D_1\rangle$ and $|D_2\rangle$,

$$H_{electronic} = \begin{pmatrix} E_{D_1} & J \\ J & E_{D_2} \end{pmatrix}, \tag{11}$$

the energy gap between the electronic excitons is given as $\Delta \epsilon_{electronic} = 895 \ cm^{-1}$, which is used as the frequency of the vibrational mode. In other words, the vibrational mode is resonant with the energy gap between the electronic excitons. We incorporate vibrational relaxation in our calculations, since the relaxation of the vibrational mode on l_2 , due to its

interaction with the bath, acts as a competing pathway to $l_2 \rightarrow l_3$ transport. The electronic and vibrational environments are both modeled by the Drude spectral density, where the reorganization energies are given as: $\lambda_{elec} = 100 \ cm^{-1}$ and $\lambda_{vib} = 10 \ cm^{-1}$. λ_{vib} , thus, corresponds to a vibrational reorganization time given as $\tau_{vib} \approx 3.3 \ ps$. The bath is considered to reside at a temperature $T = 300 \ K$ and the phonon relaxation frequency for both electronic and vibrational excitations is $\omega_c = 30 \ cm^{-1}$. We use these bath parameters for all the models. To evaluate excitation transport to the energy sink A, we choose $\Gamma_{l_3 \rightarrow A} = 1.8 \times 10^{12} \ s^{-1}$, where $\Gamma_{l_3 \rightarrow A}$ is the rate of decay of excitation from the local state l_3 to A.

A closer look at the energy level diagram for model 1 tells us that the lowest energy adiabatic state a_1 is mostly localized on the local state l_1 , with a small contribution from l_3 , and the highest energy adiabatic state a_3 is localized on the local state l_2 with a small contribution from l_3 . In contrast, the adiabatic state a_2 is more mixed, with it being localized mostly on l_3 , but with modest contributions from both l_1 and l_2 (see Table S1). Since the quantity of interest is the temporal evolution of population at l_3 , it is easy to see that the adiabatic states a_2 and a_3 will play prominent roles in dictating the dynamics, since they are mostly localized on l_3 and l_2 , respectively. Therefore, the faster the $a_3 \to a_2$ pathway is, the faster the $l_2 \to l_3$ pathway will be, since $a_3 \rightarrow a_2$ is downhill transport which has a greater relaxation rate than uphill transport. The uphill transport, nevertheless, has a sizable rate because the energy gap between a_3 and a_2 is thermally accessible at $T = 300 \ K$. The relaxation rates between pairs of adiabatic states, computed using Eqns. 9 and 10, are listed in Table 2 for the various models. Apart from the energetics, the overlap between the local and the adiabatic states, as seen in Eqns. 9 and 10, will also dictate the rate of energy transport. A larger overlap for a pair of adiabatic states with a given local state will contribute to an increased rate between the adiabatic states. Therefore, a more mixed adiabatic state that enjoys strong overlap with multiple local states is expected to boost transport. Strong electronic coupling between local states will also lead to more mixed states. Finally, the Huang Rhys factor also determines mixing to an extent, since a larger Huang Rhys factor implies a more nonlocal vibration that contributes to mixing through the off-diagonal overlap terms in Eq. 1. However, we should also note that a larger off-diagonal term will also lead to greater splittings between adiabatic states that will have an adverse effect on rates. Also, a greater mixing implies that the local states are strongly mixed to form the adiabatic states. Therefore, when we probe the population evolution at the local states, unidirectional transport between the local states is reduced since the adiabatic states are delocalized across the local states, thus enabling backtransport between the local states. Therefore, for maximum yield, the system will need to achieve the limit of optimum mixing, since this will determine both the energy splittings, and the overlap of adiabatic states with local states. Figure 3(a) depicts the local populations evolving with time for model 1, and we find that the population at l_3 increases quite rapidly and overshoots the population at l_2 before 100 fs.

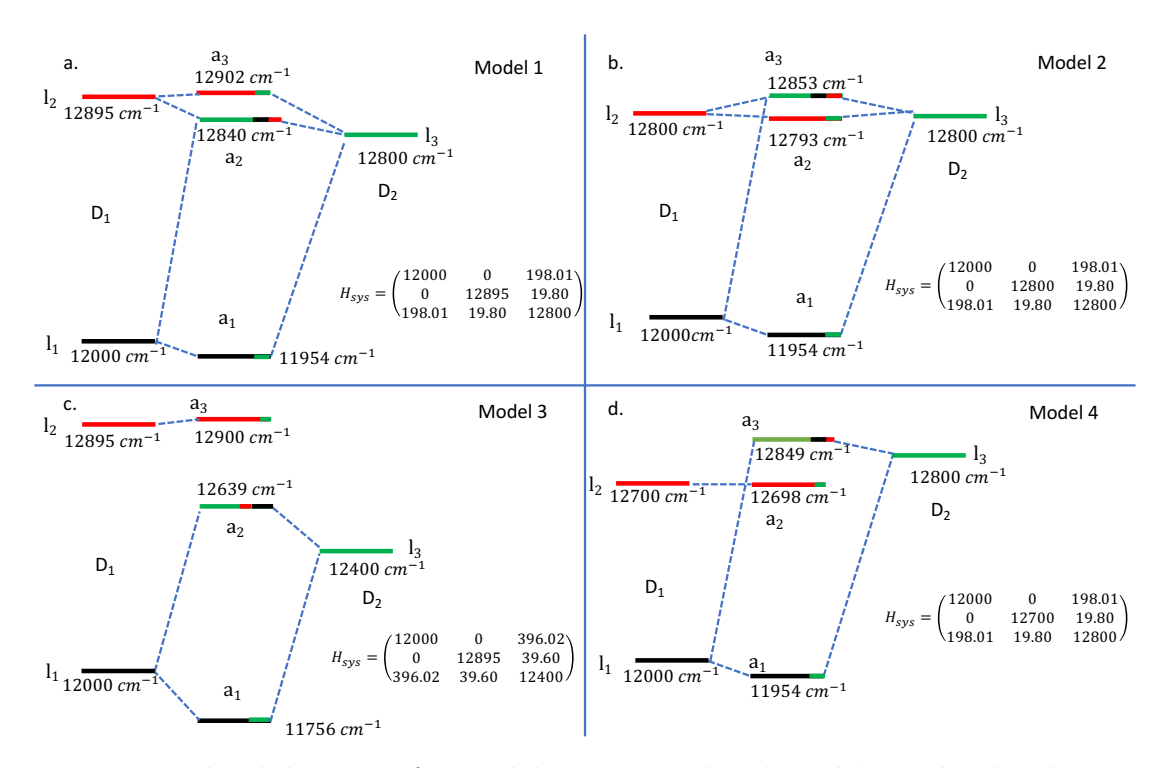


Figure 2: Energy level diagrams for models 1, 2, 3 and 4. l_1 and l_2 are localized on D_1 and label the states $|D_1v_{D_1,0'}^ev_{D_2,0}^g\rangle$ and $|D_1v_{D_1,1'}^ev_{D_2,0}^g\rangle$, respectively. l_3 is localized on D_2 and labels the state $|D_2v_{D_1,0}^gv_{D_2,0'}^e\rangle$. a_1 , a_2 and a_3 label the stationary adiabatic states, and the color coding of the adiabatic states indicates the presence of the respective local states.

We now compare the previous model with model 2, where l_2 and l_3 are degenerate, and the vibrational mode has a vibrational frequency 800 cm^{-1} which is quasi-resonant with the excitonic energy gap $\Delta \epsilon_{electronic} = 895 \ cm^{-1}$. The immediate effects can be observed in the energy level diagram for model 2 in figure 2(b). We see that the mixing in the adiabatic states a_3 and a_2 is reversed compared with model 1. a_3 is now the more mixed adiabatic state and is localized mostly on l_3 with small contributions from both l_1 and l_2 (see Table S2). a_2 is localized on l_2 , with a small contribution from l_3 . a_1 is exactly the same for both models. While the energy gap between a_3 and a_2 is almost the same as in model 1, the rates are somewhat different (see Table 2) due to the fact that the higher energy a_3 state is now the more mixed state compared to the mostly local lower energy a_2 . A second important consequence is the pathway $l_2 \to l_3$, that we are interested in for the ratcheted photophysics, is now facilitated through the uphill transport pathway $a_2 \rightarrow a_3$, and hence has a lower transport rate compared to the downhill route. However, for a bath temperature of 300 K, it is a thermally accessible pathway. A comparison of the populations at l_3 in Figure 3 for models 1 and 2 reinforces the energetic constraints of model 2, and depicts a lower thermal population at l_3 for model 2.

Table 2: Relaxation rates between the stationary adiabatic states, computed using Eqns. 9 and 10. For example, $\Gamma_{a_3\to a_1}$ measures the downhill relaxation rate from the adiabatic state a_3 to the adiabatic state a_1 . All the values in the table are to be multiplied by a factor of $10^{12}s^{-1}$.

$\times 10^{12} s^{-1}$	Model 1	Model 2	Model 3	Model 4	Model 5	Model 6
$\Gamma_{a_3 \to a_1}$	0.02	0.22	0.01	0.25	0.47	0.37
$\Gamma_{a_3 \to a_2}$	23.87	26.40	0.39	0.97	46.91	8.07
$\Gamma_{a_2 \to a_1}$	0.23	0.03	1.04	0	0.58	0.78
$\Gamma_{a_2 \to a_3}$	17.71	19.77	0.11	0.47	33.93	3.09
$\Gamma_{a_1 \to a_2}$	0	0	0.01	0	0.01	0.02
$\Gamma_{a_1 \to a_3}$	0	0	0	0	0.01	0

In model 3, we reduce the electronic energy gap between the local sites D_1 and D_2 ($\Delta E = 400 \ cm^{-1}$) and increase the electronic coupling J in Eq. 11, such that we have the

same energy gap between the electronic excitons $\Delta \epsilon_{electronic} = 895 \ cm^{-1}$, as in models 1 and 2. This is used as the frequency of the vibrational mode in the vibronic Hamiltonian for model 3 in figure 2(c), and therefore, the vibrational mode is resonant with the energy gap between the electronic excitons. A direct consequence of increasing the value of J is larger off-diagonal couplings in the vibronic Hamiltonian. The coupling between the local states l_1 and l_3 is much larger compared to that between l_2 and l_3 . Consequently, the adiabatic states a_1 and a_2 have sizable overlap with the local states l_1 and l_3 , with a_2 having a small contribution from l_2 . a_3 is predominantly localized on l_2 , with a very small contribution from l_3 due to a small, nonzero coupling between l_2 and l_3 (see Table S3). Despite the creation of more mixed states arising from a larger electronic coupling, the mixing here does not boost the transport between l_2 and l_3 , because: (a) the mixing occurs mostly between l_1 and l_3 , leading to formation of a_1 and a_2 , and possibly a somewhat boosted transport between a_2 and a_1 due to the sizable overlap between the local and adiabatic states that affect the rates (Eqns. 9 and 10); a_3 that is localized on l_2 is mostly unaffected by this mixing, and (b) compared to models 1 and 2, the energy gap between a_3 and a_2 is larger, since we reduce the energy gap between l_1 and l_3 in this model at the cost of an increased value of J and a resonant vibrational mode, resulting in lower transport rates. This study shows that while a moderate amount of mixing might promote boosted transport as in model 1, a large value of an electronic coupling, while considering a resonant vibrational mode for a given $\Delta E_{D_2,D_1}$, could actually result in slower rates between l_2 and l_3 , as in model 3. Also, as discussed earlier, a large off-diagonal coupling implies reduced unidirectional transport to l_3 . A comparison of the rates for models 1, 2 and 3 in Table 2 shows that rates for model 3 are significantly lower than those for models 1 and 2.

In models 1 and 3, we have considered vibrational modes resonant with the energy gap between electronic excitons. In model 2, the vibrational mode is quasi-resonant, however l_2 and l_3 are degenerate, resulting in closely spaced adiabatic states and therefore, sizable transport from l_2 to l_3 . In model 4, we consider a non-resonant vibrational mode with a vibrational frequency of 700 cm^{-1} while $\Delta\epsilon_{electronic} = 895 \ cm^{-1}$. We find that the adiabatic states a_1 , a_2 and a_3 are predominantly localized on l_1 , l_2 and l_3 , respectively and a_1 and a_2 have very small contributions from l_3 and l_1 , respectively (see Table S4). As a result of the negligible mixing, the term in the relaxation rates for a pair of adiabatic states in the rate equations, that arises from the overlap between the local states and the given pair of adiabatic states, is negligible and results in very small transport rates (see relaxation rates for model 4 in Table 2). Therefore, resonance/quasi-resonance is desirable since this enables the formation of mixed adiabatic states that leads to boosted transport.

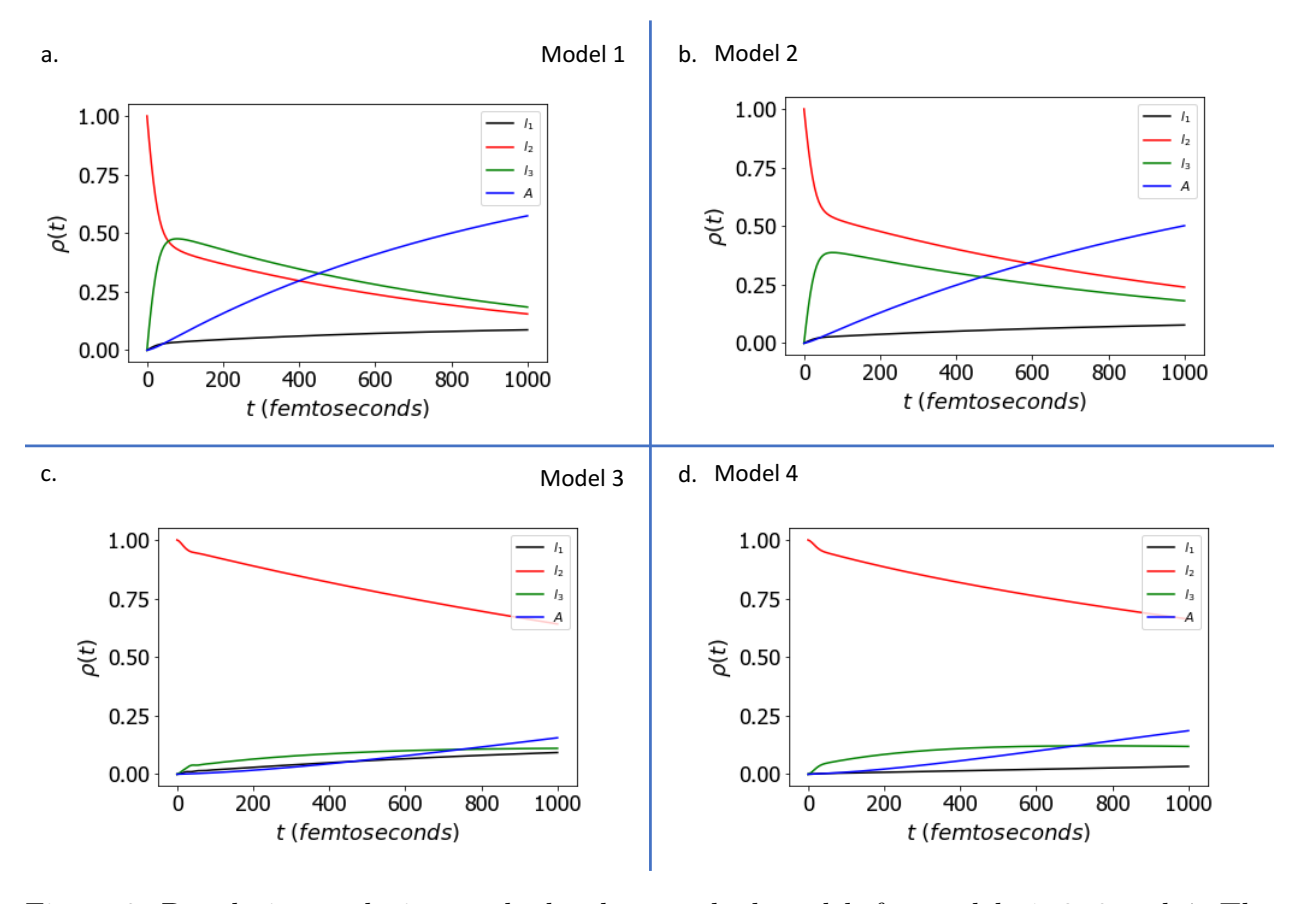


Figure 3: Population evolution at the local states l_1 , l_2 and l_3 for models 1, 2, 3 and 4. The rate of decay of excitation from l_3 to A is $\Gamma_{l_3\to A}=1.8\times 10^{12}~s^{-1}$, where A acts as an energy sink. The blue curve depicts the growth of population at A.

Models 5 and 6 differ from each other with respect to the Huang Rhys factor (0.01 for

model 5 and 0.1 for model 6, implying a more nonlocal vibrational mode). While a larger Huang-Rhys factor implies the involvement of multiple vibrational states in the dynamics, a larger vibrational basis is a subject of future study. For these models, we explore a special case where the vibrational mode frequency of $646 \text{ } cm^{-1}$ is resonant with the energy gap between the higher adiabatic state and the lower local state in the electronic-only Hamiltonian in Eq. 11. A significant consequence of this can be seen in the energy level diagrams for models 5 and 6 in Figure 4, where the adiabatic states are more strongly mixed when compared with the previous models. While the lowest adiabatic state a_1 , for both the models, is given by a superposition of l_1 and l_3 , with a stronger contribution from the lower energy local state l_1 , the higher energy adiabatic states a_2 and a_3 are strongly mixed adiabatic states, featuring sizable contributions from all the local states l_1 , l_2 and l_3 (see Tables S5 and S6). While the off-diagonal couplings between l_1 and l_3 for these two models are not too different, the off-diagonal coupling between l_2 and l_3 in model 6 is nearly three times that of the coupling in model 5, resulting in a larger splitting (= 200 cm⁻¹) between the adiabatic states a_3 and a_2 in model 6, compared to an energy splitting of 68 cm^{-1} between a_3 and a_2 , in model 5. The larger off-diagonal coupling between l_2 and l_3 in model 6 is a consequence of the larger Huang Rhys factor for model 6. From the energy level diagram, it is easy to see that the transport from l_2 to l_3 will mostly be mediated via the adiabatic states a_3 and Therefore, the larger energy splitting between a_3 and a_2 gives smaller relaxation rates for model 6, as seen from the rates in Table 2 for models 5 and 6. From the population evolution plots in figure 4, we can see that the population at l_1 grows faster for models 5 and 6, compared to the previous models. This can be attributed to the fact that the local state l_1 has presence in the adiabatic states a_3 and a_2 that feature a strong contribution from the initial seat of excitation at l_2 , that contributes to the $l_2 \to l_1$ transport. The $l_2 \to l_1$ transport is faster in model 6 compared to model 5 since the energy gap between a_2 and a_1 , where a_1 features a strong contribution from l_1 , is lesser in model 6, compared to model 5. The local state populations for model 6 exhibit oscillations at short times (up to $\approx 200 \ fs$) that gradually decohere due to interaction with the bath. The oscillations have a frequency of 200 cm^{-1} , arising from the energy gap between the adiabatic states a_3 and a_2 . The local state population at l_3 is seen to evolve similarly for models 5 and 6 at longer times, unlike the populations at l_2 and l_1 that evolve differently for the two models.

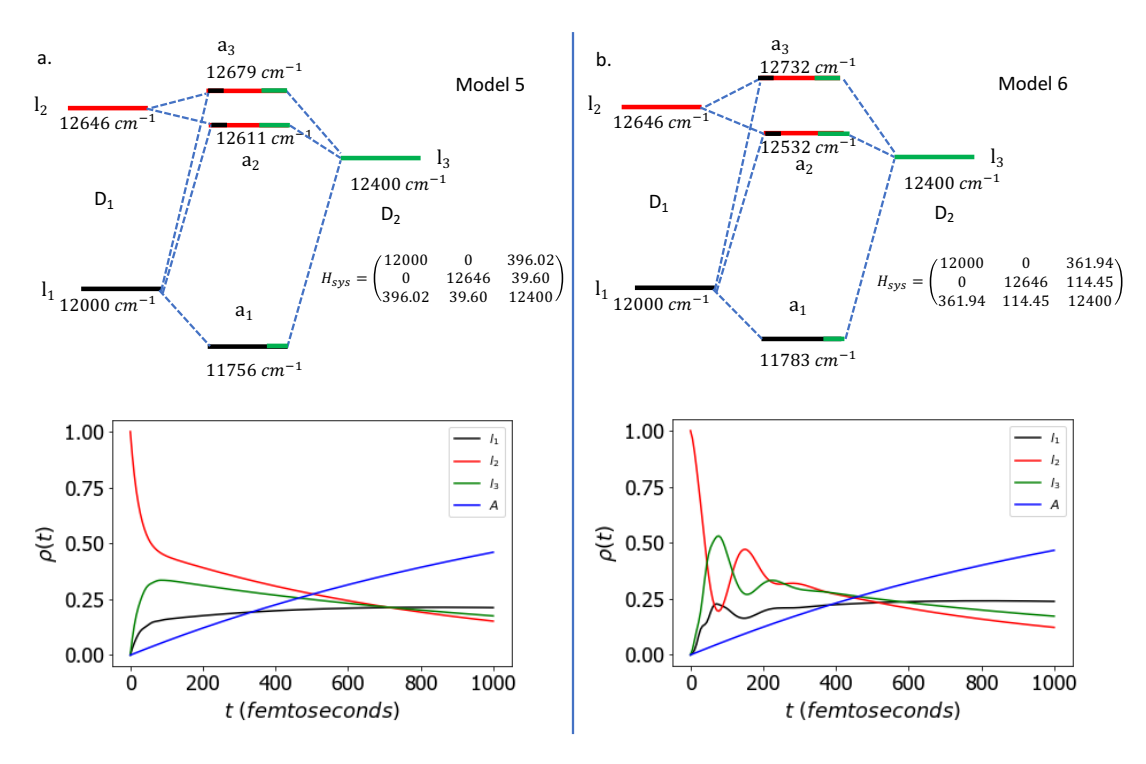


Figure 4: Energy level diagrams and population evolution at the local states l_1 , l_2 , l_3 and acceptor A, for models 5 and 6. The oscillations in the local populations in model 6 have a frequency of 200 cm^{-1} , arising from the energy gap between the stationary adiabatic states a_3 and a_2 .

Figure 5(a) compares the temporal evolution of the acceptor population for all the six models. To reiterate, l_2 , that labels $|D_1v_{D_1,1'}^ev_{D_2,0}^g\rangle$, is the initial seat of excitation localized on D_1 , while l_3 that labels $|D_2v_{D_1,0}^gv_{D_2,0'}^e\rangle$ is localized on D_2 . In our calculations, we investigate the transport from l_2 to l_3 , followed by a unidirectional decay to A, that serves as an energy sink. The rate of decay for the process is given as $\Gamma_{l_3\to A}=1.8\times 10^{12}~s^{-1}$. Transforming to the stationary adiabatic basis, the rate of decay from a stationary adiabatic state to A can be expressed in terms of the respective eigenvector components with respect

to l_3 . Model 1 is seen to result in the fastest transport at subpicosecond timescales but at longer times, models 5 and 6 take over. Given the vibrational reorganization time of $\tau_{vib} = 3.3 \ ps$, the excitation transport in model 1 outcompetes the vibrational relaxation the best, compared to the other models. It is surprising to note that the acceptor populations for models 5 and 6 grow almost together, despite markedly different relaxation rates for the two models. On the other hand, the eigenvector components that describe the overlap of the adiabatic states with the local states for both these models are almost identical. This is possibly the reason for similar acceptor populations for these two models, since the decay of population from an adiabatic state to the acceptor is described by only the eigenvector components with respect to l_3 . It is to be noted that the rate $\Gamma_{l_3\to A}$ is a key parameter that dictates the unidirectional transport. We have compared the acceptor populations for the above 6 models at $\Gamma_{l_3\to A}=9\times 10^{12}~s^{-1}$ and $\Gamma_{l_3\to A}=0.45\times 10^{12}~s^{-1}$, in figures S1-S2. A larger value of $\Gamma_{l_3\to A}$ is seen to result in a faster growth at A for all models. For $\Gamma_{l_3 \to A} = 9 \times 10^{12} \ s^{-1}$, the transfer of population to A is extremely rapid for models 1, 2, 5 and 6, compared to $\Gamma_{l_3\to A}=0.45\times 10^{12}~s^{-1}$. Figure 5(b) depicts the acceptor population at 4 ps for all the models, plotted with respect to the electronic coupling J and $\Delta\Omega$, that denotes the shift of the vibrational frequency Ω from the electronic-only stationary adiabatic energy gap between the S_1 states of D_1 and D_2 in Eq. 11. The Huang Rhys parameter σ is not included as a coordinate since the acceptor populations are seen to grow almost together for models that differ with respect to σ . It is noted that resonance/quasi-resonance, along with moderate J is desirable for enhanced transport to A. However, models 5 and 6, despite having $\Delta\Omega = 249 \text{ cm}^{-1}$, lead to fastest transport to A at longer times. The reason for this is that they explore a special resonance regime where the vibrational frequency is resonant with the energy gap between the higher adiabatic state and the lower local state in the electronic-only Hamiltonian in Eq. 11, that leads to optimally mixed adiabatic states and a boosted transport.

In the discussion above, we demonstrate that the system needs to achieve an optimum

balance between electronic coupling, Huang Rhys mixing and resonance of the vibrational mode, to optimize $l_2 \rightarrow l_3$ transport. Among all the models that we discuss, model 1 is best suited for a fast transport to l_3 at subpicosecond timescales. While it enjoys a resonant vibrational mode, the electronic coupling between D_1 and D_2 is about half of the electronic coupling considered in model 3. An optimum electronic coupling is desirable for formation of mixed adiabatic states that can boost rates, since the rates feature an overlap between the local and adiabatic states. However, a very large electronic coupling in the presence of a resonant mode could have an adverse effect on transport as it diminishes unidirectional transport since the adiabatic states are now delocalized across the local states. On the other hand, if the vibrational mode is resonant/quasi-resonant with the energy gap between the higher adiabatic state and the lower local state in the electronic-only Hamiltonian, as seen in models 5 and 6, it explores a special regime where we have strongly mixed adiabatic states due to this specific form of resonance. Such models lead to enhanced transport. If the vibration is described by a large Huang Rhys factor, as in model 6, coherent oscillations could be observed at shorter timescales that eventually decohere. A faster $l_2 \rightarrow l_3$ transport leads to a quicker growth of the acceptor population. Therefore, models 1, 2, 5 and 6 are best suited for an efficient transport to A. It is important to note that though different values of Huang Rhys parameters, for given values of J and $\Delta\Omega$, result in markedly different local state evolutions, they result in similar growth at A, as seen for models 5 and 6. While the calculations discussed in this work focus on energy transport, we can expect similar principles to apply to ratcheted electron transport. This is a subject of future research.

Acknowledgement

This work was inspired by discussions with colleagues at CSQC (Center for Synthesizing Quantum Coherence), that is supported by the National Science Foundation under Grant no. 1925690. P.B. was supported by the U.S. Department of Energy, Office of Science,

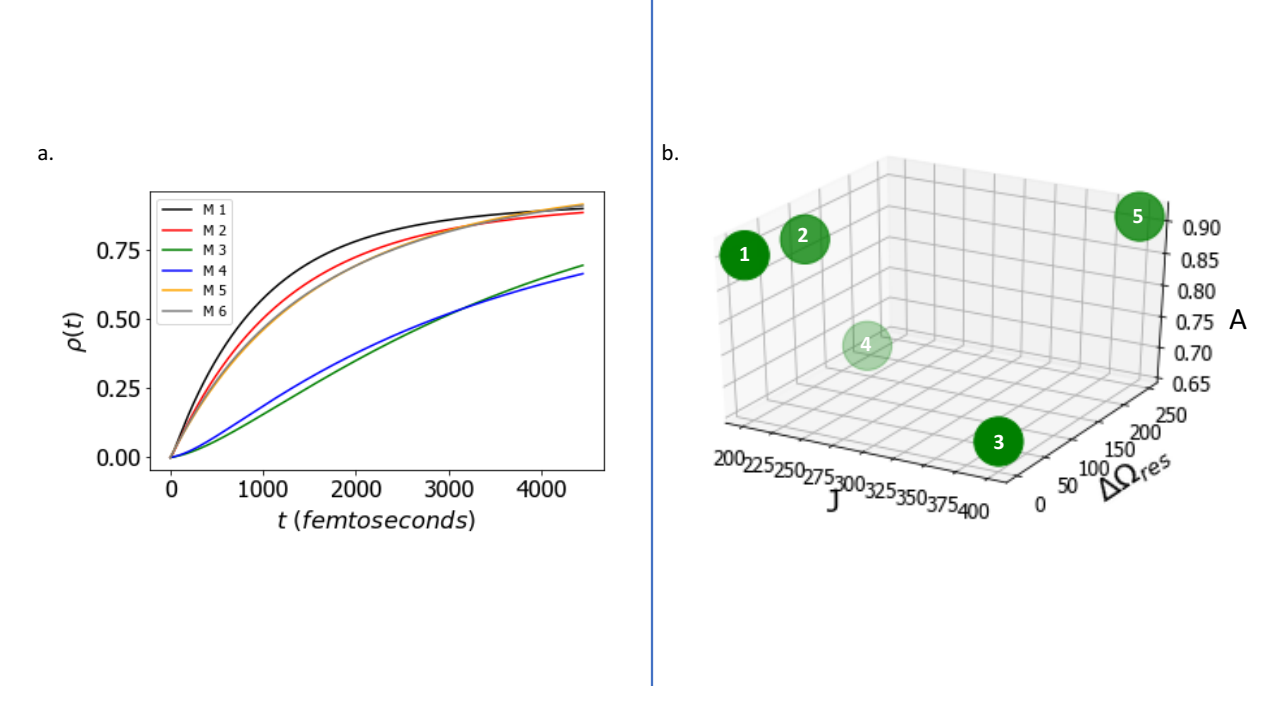


Figure 5: (a) A comparison of the acceptor populations for the six models discussed in our paper and designated as M 1-M 6, given that the rate of decay of excitation from l_3 to A is $\Gamma_{l_3\to A}=1.8\times 10^{12}~s^{-1}$. The growth of population at A is almost identical for models 5 and 6, that differ from each other with respect to the Huang Rhys factor (0.01 for model 5 and 0.1 for model 6), despite the markedly different local state populations, as seen in figure 4, and relaxation rates, listed in Table 2. Model 1 is seen to result in the fastest transport to A for subpicosecond timescales, followed by model 2. At longer times, models 5 and 6 take over. (b) The acceptor population at 4 ps, depicted by the z-axis label A, is plotted with respect to the electronic coupling parameters J, and $\Delta\Omega$, that denotes the shift of the vibrational frequency Ω from the electronic-only stationary adiabatic energy gap between the S_1 states of D_1 and D_2 , for models 1-5. Model 6 is not included explicitly since the acceptor population in model 6 has an almost identical evolution as in model 5, that differ with respect to the Huang Rhys factor. The Huang Rhys parameter σ is not included as a coordinate since the acceptor populations are seen to almost together for models that differ only with respect to σ .

Chemical Sciences, Geosciences, and Biosciences Division and the work utilized resources of the National Energy Research Computing Center (NERSC), a U.S. Department of Energy, Office of Science User Facility operated under contract No. DE-AC02-05CH11231.

Supporting Information

Tables S1-S6: Contributions of the local states, l_1 , l_2 and l_3 , to the adiabatic states a_1 , a_2 and a_3 for the six models discussed in the main manuscript. Figures S1-S2: Comparison of the acceptor populations for the six models discussed in the main manuscript for different values of $\Gamma_{l_3\to A}$: (a) $\Gamma_1 = 9 \times 10^{12} \ s^{-1}$, (b) $\Gamma_2 = 1.8 \times 10^{12} \ s^{-1}$ and (c) $\Gamma_3 = 0.45 \times 10^{12} \ s^{-1}$.

References

- Ishizaki, A.; Fleming, G. R. Theoretical examination of quantum coherence in a photosynthetic system at physiological temperature. *Proceedings of the National Academy of Sciences* 2009, 106, 17255–17260.
- (2) Roden, J. J.; Bennett, D. I. G.; Whaley, K. B. Long-range energy transport in photosystem II. *The Journal of Chemical Physics* **2016**, *144*, 245101.
- (3) Mohseni, M.; Rebentrost, P.; Lloyd, S.; Aspuru-Guzik, A. Environment-assisted quantum walks in photosynthetic energy transfer. The Journal of Chemical Physics 2008, 129, 174106.
- (4) Womick, J. M.; Moran, A. M. Vibronic Enhancement of Exciton Sizes and Energy Transport in Photosynthetic Complexes. The Journal of Physical Chemistry B 2011, 115, 1347–1356.
- (5) Fujihashi, Y.; Higashi, M.; Ishizaki, A. Intramolecular Vibrations Complement the

- Robustness of Primary Charge Separation in a Dimer Model of the Photosystem II Reaction Center. *The Journal of Physical Chemistry Letters* **2018**, *9*, 4921–4929.
- (6) Stones, R.; Olaya-Castro, A. Vibronic Coupling as a Design Principle to Optimize Photosynthetic Energy Transfer. *Chem* **2016**, *1*, 822 824.
- (7) Halpin, A.; Johnson, P. J. M.; Tempelaar, R.; Murphy, R. S.; Knoester, J.; Jansen, T. L. C.; Miller, R. J. D. Two-dimensional spectroscopy of a molecular dimer unveils the effects of vibronic coupling on exciton coherences. *Nature Chemistry* 2014, 6, 196.
- (8) Chin, A. W.; Prior, J.; Rosenbach, R.; Caycedo-Soler, F.; Huelga, S. F.; Plenio, M. B. The role of non-equilibrium vibrational structures in electronic coherence and recoherence in pigment–protein complexes. *Nature Physics* **2013**, *9*, 113.
- (9) Dijkstra, A. G.; Wang, C.; Cao, J.; Fleming, G. R. Coherent Exciton Dynamics in the Presence of Underdamped Vibrations. The Journal of Physical Chemistry Letters 2015, 6, 627–632, PMID: 26262477.
- (10) Bennett, D. I. G.; Malý, P.; Kreisbeck, C.; van Grondelle, R.; Aspuru-Guzik, A. Mechanistic Regimes of Vibronic Transport in a Heterodimer and the Design Principle of Incoherent Vibronic Transport in Phycobiliproteins. The Journal of Physical Chemistry Letters 2018, 9, 2665–2670, PMID: 29683676.
- (11) Bhattacharyya, P.; Fleming, G. R. The role of resonant nuclear modes in vibrationally assisted energy transport: The LHCII complex. *The Journal of Chemical Physics* **2020**, 153, 044119.
- (12) Lin, V.; DiMagno, S.; Therien, M. Highly conjugated, acetylenyl bridged porphyrins: new models for light-harvesting antenna systems. *Science* **1994**, *264*, 1105–1111.
- (13) Lin, V. S.-Y.; Therien, M. J. The Role of Porphyrin-to-Porphyrin Linkage Topology in the Extensive Modulation of the Absorptive and Emissive Properties of a Series of

- Ethynyl- and Butadiynyl-Bridged Bis- and Tris(porphinato)zinc Chromophores. *Chemistry A European Journal* **1995**, *1*, 645–651.
- (14) Angiolillo, P. J.; Lin, V. S.-Y.; Vanderkooi, J. M.; Therien, M. J. EPR Spectroscopy and Photophysics of the Lowest Photoactivated Triplet State of a Series of Highly Conjugated (Porphinato)Zn Arrays. *Journal of the American Chemical Society* 1995, 117, 12514–12527.
- (15) Kumble, R.; Palese, S.; Lin, V. S.-Y.; Therien, M. J.; Hochstrasser, R. M. Ultrafast Dynamics of Highly Conjugated Porphyrin Arrays. *Journal of the American Chemical Society* 1998, 120, 11489–11498.
- (16) Shediac, R.; Gray, M. H. B.; Uyeda, H. T.; Johnson, R. C.; Hupp, J. T.; Angio-lillo, P. J.; Therien, M. J. Singlet and Triplet Excited States of Emissive, Conjugated Bis(porphyrin) Compounds Probed by Optical and EPR Spectroscopic Methods. *Journal of the American Chemical Society* 2000, 122, 7017–7033.
- (17) Fletcher, J. T.; Therien, M. J. Extreme Electronic Modulation of the Cofacial Porphyrin Structural Motif. *Journal of the American Chemical Society* 2002, 124, 4298–4311, PMID: 11960459.
- (18) Susumu, K.; Therien, M. J. Decoupling Optical and Potentiometric Band Gaps in π-Conjugated Materials. Journal of the American Chemical Society 2002, 124, 8550– 8552, PMID: 12121095.
- (19) Duncan, T. V.; Susumu, K.; Sinks, L. E.; Therien, M. J. Exceptional Near-Infrared Fluorescence Quantum Yields and Excited-State Absorptivity of Highly Conjugated Porphyrin Arrays. *Journal of the American Chemical Society* 2006, 128, 9000–9001, PMID: 16834350.
- (20) Kang, Y. K.; Zhang, P.; Rubtsov, I. V.; Zheng, J.; Bullard, G.; Beratan, D. N.; Therien, M. J. Orientational Dependence of Cofacial Porphyrin–Quinone Electronic In-

- teractions within the Strong Coupling Regime. The Journal of Physical Chemistry B **2019**, 123, 10456–10462, PMID: 31710233.
- (21) Rawson, J.; Stuart, A. C.; You, W.; Therien, M. J. Tailoring Porphyrin-Based Electron Accepting Materials for Organic Photovoltaics. *Journal of the American Chemical Society* 2014, 136, 17561–17569, PMID: 25415459.
- (22) Bhattacharyya, P.; Sebastian, K. L. Adiabatic eigenfunction-based approach for coherent excitation transfer: An almost analytical treatment of the Fenna-Matthews-Olson complex. *Phys. Rev. E* **2013**, *87*, 062712.
- (23) Bhattacharyya, P.; Sebastian, K. L. Adiabatic Eigenfunction Based Approach to Coherent Transfer: Application to the Fenna–Matthews–Olson (FMO) Complex and the Role of Correlations in the Efficiency of Energy Transfer. The Journal of Physical Chemistry A 2013, 117, 8806–8813, PMID: 23805909.
- (24) Bhattacharyya, P.; Fleming, G. R. Two-Dimensional Electronic-Vibrational Spectroscopy of Coupled Molecular Complexes: A Near-Analytical Approach. The Journal of Physical Chemistry Letters 2019, 10, 2081–2089.